Evaluation of Scalar Advection Schemes in the Advanced Research WRF Model Using Large-Eddy Simulations of Aerosol–Cloud Interactions

HAILONG WANG

Cooperative Institute for Research in Environmental Sciences, University of Colorado, Boulder, and NOAA/Earth System Research Laboratory, Boulder, Colorado

WILLIAM C. SKAMAROCK

National Center for Atmospheric Research, Boulder, Colorado*

GRAHAM FEINGOLD

NOAA/Earth System Research Laboratory, Boulder, Colorado

(Manuscript received 2 October 2008, in final form 18 February 2009)

ABSTRACT

In the Advanced Research Weather Research and Forecasting Model (ARW), versions 3.0 and earlier, advection of scalars was performed using the Runge–Kutta time-integration scheme with an option of using a positive-definite (PD) flux limiter. Large-eddy simulations of aerosol–cloud interactions using the ARW model are performed to evaluate the advection schemes. The basic Runge–Kutta scheme alone produces spurious oscillations and negative values in scalar mixing ratios because of numerical dispersion errors. The PD flux limiter assures positive definiteness but retains the oscillations with an amplification of local maxima by up to 20% in the tests. These numerical dispersion errors contaminate active scalars directly through the advection process and indirectly through physical and dynamical feedbacks, leading to a misrepresentation of cloud physical and dynamical processes. A monotonic flux limiter is introduced to correct the generally accurate but dispersive solutions given by high-order Runge–Kutta scheme. The monotonic limiter effectively minimizes the dispersion errors with little significant enhancement of numerical diffusion errors. The improvement in scalar advection using the monotonic limiter is discussed in the context of how the different advection schemes impact the quantification of aerosol–cloud interactions. The PD limiter results in 20% (10%) fewer cloud droplets and 22% (5%) smaller cloud albedo than the monotonic limiter under clean (polluted) conditions. Underprediction of cloud droplet number concentration by the PD limiter tends to trigger the early formation of precipitation in the clean case, leading to a potentially large impact on cloud albedo change.

1. Introduction

As a fundamental process in fluid dynamics, advection is of central importance in the transport of energy, water, and chemical species. In atmospheric modeling, numerical diffusion and dispersion errors induced by the treatment of advection can affect the representation of physical processes. Sharp gradients and discontinuities in scalar quantities, such as cloud condensation nuclei (CCN) number concentration, cloud water mass, and droplet number concentration, make the numerical treatment of advection especially challenging. Without adequate treatment of this problem, either unacceptable numerical diffusion or spurious oscillation can appear near sharp gradients in the scalars (e.g., cloud edges). As a result, simulations of physical processes associated with aerosol–cloud–precipitation interactions could be ambiguous or misleading. Hence, when numerically modeling advection, our goal is to minimize diffusion and dispersion errors while maintaining scheme stability and efficiency.

---

* The National Center for Atmospheric Research is sponsored by the National Science Foundation.

Corresponding author address: Hailong Wang, 325 Broadway, R/CSD2, Boulder, CO 80305.
E-mail: hailong.wang@noaa.gov

DOI: 10.1175/2009MWR2820.1

Two concepts, positive definiteness and monotonicity, are closely related to these numerical errors. Positive definiteness assures positive scalar mixing ratios, while monotonicity means that the numerical advection scheme does not generate new local minima and maxima. Spurious oscillations near sharp gradients due to dispersion error can generate nonphysical negative mixing ratios and new extrema in transported scalars. In the Advanced Research Weather Research and Forecasting Model (ARW), versions 3.0 and earlier, the advection of scalars is performed using the third-order Runge–Kutta (RK) time-integration scheme (Skamarock et al. 2008) with second- through sixth-order accuracy options for evaluation of the advective fluxes. The even-order options contain no implicit numerical diffusion, while the odd-order options are inherently diffusive with a diffusion term proportional to the Courant number. However, the even-order options tend to be more dispersive (e.g., Anderson and Fattahi 1974). The basic RK advection scheme is neither positive-definite (PD) nor monotonic. The scheme conserves scalar mass if negative mixing ratios are retained. However, in most physical processes negative mixing ratios are not allowed and, hence, simply removing them (setting negative mixing ratios to zero where they occur) adds a spurious scalar mass source. To avoid this situation, a PD flux limiter (Zalesak 1979; Skamarock 2006) has been introduced into the ARW beginning with the version-2.2 release in 2006. It is applied, when necessary, to renormalize outgoing fluxes from the targeted grid box calculated by the basic RK scheme. Improvement in high-resolution precipitation forecasts with this PD flux limiter has been demonstrated by Skamarock and Weisman (2009). Nonetheless, the PD flux limiter does not assure monotonicity. For cloud-resolving modeling studies and many other applications it is often desirable to use a monotonic advection scheme for scalar transport.

Cloud-resolving modeling or large-eddy simulation (LES) has proven to be a powerful tool to advance our understanding of cloud physics, turbulent dynamics, and aerosol–cloud interactions unavailable from observations. By design, the ARW is suitable for use in a broad spectrum of applications spanning scales from meters to the global scale (Skamarock et al. 2008). Moeng et al. (2007) explored the suitability of the ARW for large-eddy simulation of the planetary boundary layer (PBL). With some improvements to the model, they showed that model simulations of PBL turbulence are statistically comparable to observations, laboratory data, and those of other LES studies. However, they did not perform simulations of PBL clouds primarily because the PD flux limiter was not available in the earlier version (ARW version 2.1) of the model (C.-H. Moeng 2007, personal communication). We emphasize the suitability of the ARW for cloud-resolving modeling applications not only because it can potentially perform as well as other LES models, but also because it has two major advantages. First, it has the option of coupling with an integrated aerosol chemistry package (Grell et al. 2005), which allows for a more realistic representation of the aerosol budget. Second, it has the capability of two-way grid nesting, which allows for cross-scale interactions between turbulent motion and mesoscale organization when running multiscale simulations with an LES domain embedded in a mesoscale domain. This enables real case studies rather than idealized simulations with initially homogeneous meteorology and periodic boundary conditions. Moeng et al. (2007) also examined the two-way nesting capability of the ARW, but again, limited by the advection scheme, the study only considered dry convection.

In this study, a monotonic flux limiter (Zalesak 1979; Skamarock 2006), which was not available in previously released versions of the ARW, is formulated and applied to the basic RK advection scheme. Its performance is evaluated against the basic RK scheme and the PD flux limiter by examining the advection of passive tracers, CCN, and cloud droplets in three-dimensional large-eddy simulations of a stratocumulus-capped boundary layer. The significance of improvement in scalar advection by the monotonic limiter is discussed in the context of how the different advection schemes impact the quantification of aerosol–cloud interactions.

2. Formulation of a monotonic flux limiter for the ARW-WRF model

The formulation of the monotonic advection scheme using a flux-correction method in the ARW-WRF follows Zalesak (1979) and Skamarock (2006), using a low-order monotonic flux limiter to correct solutions given by a high-order advection scheme that are accurate in general, but dispersive near sharp gradients. Here we describe how to apply this concept to the basic RK time-integration scheme in the ARW. For a scalar mixing ratio ϕ, the conservation equation can be written as

$$\frac{\partial \mu\phi}{\partial t} + \frac{\partial \mu u\phi}{\partial x} + \frac{\partial \mu v\phi}{\partial y} + \frac{\partial \mu\dot{\eta}\phi}{\partial \eta} = \mu S_{\phi}, \qquad (1)$$

where μ is the column mass of dry air and S_{ϕ} denotes the source/sink term (i.e., the physical tendencies and explicit mixing). The RK scheme in the ARW integrates Eq. (1) and computes the solution $(\mu\phi)^{t+\Delta t}$ in the following three steps:

$$(\mu\phi)^{t+\Delta t/3} = (\mu\phi)^t - \frac{\Delta t}{3}\left(\sum_i \delta_{x_i} F^t_{x_i} - \mu S^t_\phi\right), \tag{2a}$$

$$(\mu\phi)^{t+\Delta t/2} = (\mu\phi)^t - \frac{\Delta t}{2}\left(\sum_i \delta_{x_i} F^{t+\Delta t/3}_{x_i} - \mu S^t_\phi\right), \tag{2b}$$

and

$$(\mu\phi)^{t+\Delta t} = (\mu\phi)^t - \Delta t\left(\sum_i \delta_{x_i} F^{t+\Delta t/2}_{x_i} - \mu S^t_\phi\right), \tag{2c}$$

where $\delta_{x_i} F_{x_i}$ denotes the centered flux divergence in the ith coordinate direction at the time step indicated by the superscript of flux F_{x_i}. When using the monotonic flux limiter, the final RK step Eq. (2c) is replaced by

$$(\mu\phi)^{t+\Delta t} = (\mu\phi)^* - \Delta t \sum_i \delta_{x_i}[F^{1*}_{x_i} + R(F^{\text{cor}}_{x_i})], \tag{3a}$$

where

$$(\mu\phi)^* = (\mu\phi)^t + \Delta t\, \mu S^t_\phi. \tag{3b}$$

Here $F^{1*}_{x_i}$ is the first-order upwind flux computed using $(\mu\phi)^*$ in Eq. (3b), and the high-order flux correction $F^{\text{cor}}_{x_i}$ is calculated as the difference between this first-order upwind flux and the full high-order flux:

$$F^{\text{cor}}_{x_i} = F^{t+\Delta t/2}_{x_i} - F^{1*}_{x_i}. \tag{4}$$

The renormalized high-order flux correction $R(F^{\text{cor}}_{x_i})$ is obtained through the following procedure. First, starting from the partial update $(\mu\phi)^*$ in Eq. (3b), the first-order upwind solution is computed as

$$\widetilde{(\mu\phi)} = (\mu\phi)^* - \Delta t \sum_i \delta_{x_i} F^{1*}_{x_i}. \tag{5}$$

This solution is monotonic and positive definite. Next, recognizing that only outgoing fluxes reduce scalar mass in a volume and only incoming fluxes increase it, lower and upper bounds for the updated mass are computed as

$$\widetilde{(\mu\phi)}^{t+\Delta t}_{\min} = \widetilde{(\mu\phi)} - \Delta t \sum_i \delta_{x_i} (F^{\text{cor}}_{x_i})^+ \quad \text{and} \tag{6a}$$

$$\widetilde{(\mu\phi)}^{t+\Delta t}_{\max} = \widetilde{(\mu\phi)} - \Delta t \sum_i \delta_{x_i} (F^{\text{cor}}_{x_i})^-, \tag{6b}$$

where $(\cdot)^+$ and $(\cdot)^-$ denote outgoing and incoming flux, respectively. Finally, the flux corrections are renormalized using

$$R(F^{\text{cor}}_{x_i})^+ = (F^{\text{cor}}_{x_i})^+ \min\left[1.0, \frac{\tilde{\phi} - \phi_{\min}}{\tilde{\phi} - (\tilde{\phi})^{t+\Delta t}_{\min}}\right] \tag{7a}$$

and

$$R(F^{\text{cor}}_{x_i})^- = (F^{\text{cor}}_{x_i})^- \min\left[1.0, \frac{\tilde{\phi} - \phi_{\max}}{\tilde{\phi} - (\tilde{\phi})^{t+\Delta t}_{\max}}\right], \tag{7b}$$

where $\phi_{\max}$ and $\phi_{\min}$ are maximum and minimum scalar mixing ratios in the central and all neighboring upwind cells at time t. The renormalized fluxes are used in the update to (3a) to complete the update.

When applying the monotonic flux limiter, the application of the limiter can be viewed as replacing the flux divergence $\delta_{x_i} F^{t+\Delta t/2}_{x_i}$ in (2) by

$$\delta_{x_i}[rF^{t+\Delta t/2}_{x_i} + (1 - r)F^{1*}_{x_i}]. \tag{8}$$

The original high-order flux $F^{t+\Delta t/2}_{x_i}$ is corrected by the first-order flux $F^{1*}_{x_i}$ with a factor r, which is less than or equal to 1. The above renormalization procedure determines the factor for each flux. If monotonicity has been preserved by the basic RK scheme, then $r = 1$ and no flux correction occurs.

3. Numerical experiments to evaluate the advection schemes

Large-eddy simulations of marine stratocumulus clouds are performed using the ARW (version 3.0) model including the treatment of aerosol–cloud–precipitation interactions. Initialization of model simulations is based on nocturnal measurements made during research flight RF02 of the second Dynamics and Chemistry of Marine Stratocumulus (DYCOMS-II) field campaign (Stevens et al. 2003; Ackerman et al. 2009). The initial inversion base is at about 800 m. Total water mixing ratio q_t decreases from 9.45 g kg^{-1} in the boundary layer to about 5 g kg^{-1} near the inversion top, and potential temperature θ increases from 288.3 to 296.7 K across the inversion. The initial wind is from the northwest at 10 m s^{-1} with no shear. As surface boundary conditions, the upward surface sensible and latent heat fluxes are fixed at measured values of 16 and 93 W m^{-2}, respectively, and the surface friction velocity is fixed at 0.25 m s^{-1}. Radiative forcing is computed at every time step, in each model column, using the simple model of net longwave radiative flux following Stevens et al. (2005). Large-scale subsidence warming and drying are taken into account by assuming a uniform large-scale horizontal divergence of 3.75×10^{-6} s^{-1}.

A double-moment warm-rain microphysical scheme initially developed by Feingold et al. (1998) has been modified and incorporated in the ARW. This scheme uses lognormal basis functions to represent CCN, cloud droplet, and drizzle drop spectra. Supersaturation is calculated in a similar fashion to the bin method so that activation can be simulated. Lookup tables are generated a priori for drop collection using a stochastic collection bin model. Cloud and rain drop sedimentation is also size dependent and based on the bin method. This allows drops in each bin to fall at the appropriate velocity. Cloud optical depth and albedo at visible wavelengths are calculated in the microphysical scheme following Feingold et al. (1997).

Eight numerical experiments (RK53c, PD53c, MO53c, RK64c, PD64c, MO64c, PD53p, and MO53p) are designed to evaluate the basic RK advection scheme and the two flux limiters, and to study the impact of different flux limiters on cloud physical processes associated with aerosol–cloud interactions. In the experiment names, "RK," "PD," and "MO" indicate use of the basic RK advection with no limiter, with the PD limiter and with the monotonic limiter, respectively. The horizontal flux calculation is accurate to fifth (sixth) order and the vertical to third (fourth) order, as denoted by "53" ("64"). Experiments are conducted in either a clean ("c") or a polluted ("p") marine boundary layer.

The initial CCN number concentration[1] was assumed to be 200 (500) mg^{-1} for the entire model domain under clean (polluted) conditions. Aside from transport, activation of cloud droplets is the only sink, and evaporation of drops is the only source of CCN. No replenishing source is used. Hence, only drop collection and precipitation can deplete CCN. The microphysical scheme has separate prognostic equations for CCN, and mass and number concentration of cloud droplets and rain drops. These scalars are advected independently. We recognize that the independent advection of CCN and drops does not guarantee that the relationship between these variables is conserved (Ovtchinnikov and Easter 2009). This issue is not addressed here. In each experiment, the same advection scheme is applied to the subgrid-scale turbulent kinetic energy (TKE) as is applied to moisture species and other scalars. TKE closure is used to calculate the subgrid-scale scalar diffusion. Simulations are performed in a $10 \times 10 \times 1.5$ km^3 domain with a uniform grid spacing of 100 m in the horizontal and ~30 m in the vertical. Periodic boundary conditions are assumed in both the x and y directions. A damping layer is employed in the upper 250 m to minimize the accumulation of gravity wave energy. Given the wind speed of about 10 m s^{-1} and the time step of 1 s, the typical Courant number is about 0.1.

The use of the DYCOMS-II sounding has the benefit of testing the Weather Research and Forecasting Model (WRF) in LES mode for a cloudy boundary layer, for well-known input conditions, since results can be compared to Ackerman et al. (2009). Our initial conditions diverge from those in the Ackerman et al. (2009) intercomparison study, in that we assumed no wind shear, and modified the CCN concentrations to illustrate advection effects on aerosol–cloud interactions. However, as shown in the appendix A, comparison of base-case results of numerous fields such as total water mixing ratio, liquid water mixing ratio, liquid water potential temperature, liquid water path (LWP), cloud fraction, variance of vertical velocity, TKE, buoyancy flux, and so on, with those in the aforementioned study show that WRF-LES produces results that are similar to other LES model results.

4. Results

a. *Advection of passive tracers*

Passive tracers were initially homogeneously distributed in four cubes with a mixing ratio of 1 and 0 elsewhere in the model domain. Each cube is $2.5 \times 2.5 \times 0.9$ km^3 in volume, with the cube base at 0.3 km. Figure 1 shows the horizontal cross sections of the tracer mixing ratio field 10 min into the simulation. At this time, turbulence and mixing has not developed to the height of 750 m as indicated by the turbulent kinetic energy field (not shown), so the passive tracers are only influenced by advection. As expected, without any flux limiter the basic RK advection scheme produces significant spurious oscillations throughout the domain. Overshoots accompany the undershooting negative values to achieve domain-wide conservation. Negative tracer mixing ratios are produced both inside and outside of the tracer cubes, more significantly near the sharp gradients, with an amplitude of up to 20% of the initial value. The PD flux limiter removes negative values, but oscillations still exist near and inside the cubes. The local maxima inside the cubes are amplified by up to 20%. The structure of tracer mixing ratio in the cubes in PD53c resembles that in RK53c because the flux limiter is not applied when negative values are not produced. The monotonic limiter not only prevents negative tracer values, but also effectively eliminates oscillations and preserves the sharp gradients quite well. In MO53c, areas covered by the second color (0.0–0.01) have mixing ratios on the order from 10^{-13} to 10^{-8}, which are accurate to machine round-off. When the advection schemes with higher, even-order accuracy are

---

[1] In all calculations, CCN and drop number concentration units of number per mass are used to remove ambiguities associated with changes in volume. Here we use units of mg^{-1}, which is equivalent to cm^{-3} when air density is 1 kg m^{-3}. While it is not strictly correct to refer to this as a "concentration," we do so to avoid unfamiliar terminology such as "number mixing ratio."

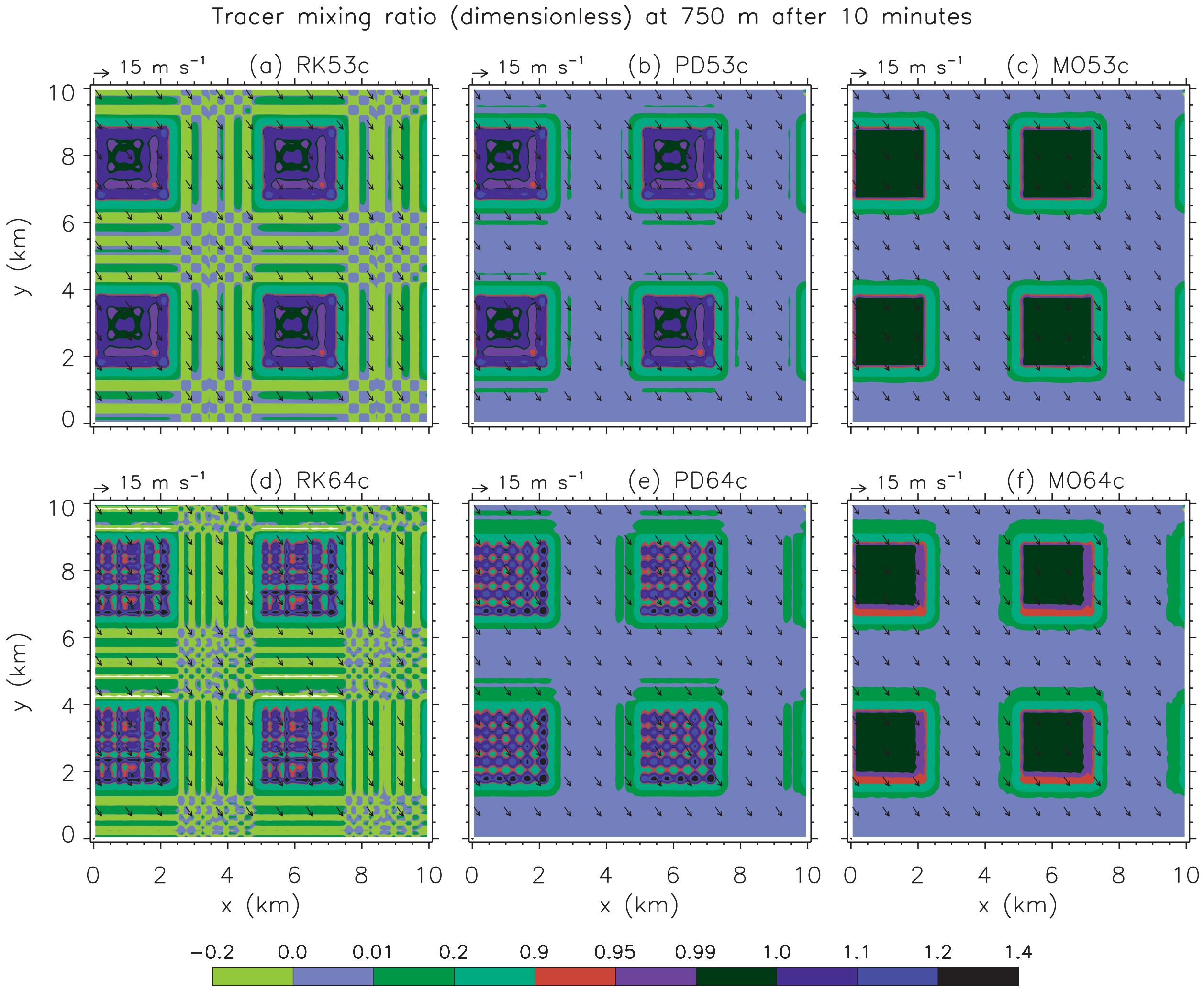

FIG. 1. Horizontal cross sections of tracer mixing ratio at about 750 m after 600 time steps (10 min) with superimposed wind vectors for experiments indicated by subtitles. Each color represents a mixing ratio bin with boundaries indicated by the color bar labels. Note that the bins are not uniformly distributed.

applied, numerical dispersion errors are larger than in corresponding lower odd-order ones. The ripple waves of tracer mixing ratio become stronger and shorter. Moreover, in the MO64c case even the monotonic limiter does not perform as well as in MO53c. Numerical diffusion errors are clearly seen at the upwind side and inside of the tracer cubes. This is very likely because more weight (a smaller r factor) has to be applied to the first-order flux in (8) when doing flux renormalization to correct the higher dispersion errors, as in the RK64c case. As a result, notable numerical diffusion errors are induced. These results indicate that the fifth- (third) order horizontal (vertical) approximation for spatial derivatives performs better than the sixth- (fourth) order scheme. Hereinafter, for simplicity, we focus on results in simulations with the fifth- (third) order horizontal (vertical) approximation.

b. *Advection of cloud species*

Like the tracers, a similar response of the CCN and cloud droplet number concentrations to the different advection schemes is observed. However, because these scalars are actively involved in physical processes, it is difficult to interpret comparisons of instantaneous fields in a point-by-point manner as given for the passive tracers in Fig. 1, hence, we present some statistical comparisons here. Figure 2 shows the frequency distribution of CCN number concentration N_c and cloud droplet plus rain drop number concentration N_d at the end of the second and fourth simulation hour. For the CCN histogram, the peak at the low-concentration end is contributed by in-cloud grid cells where most CCN have been activated to cloud droplets, and the peak at the high-concentration

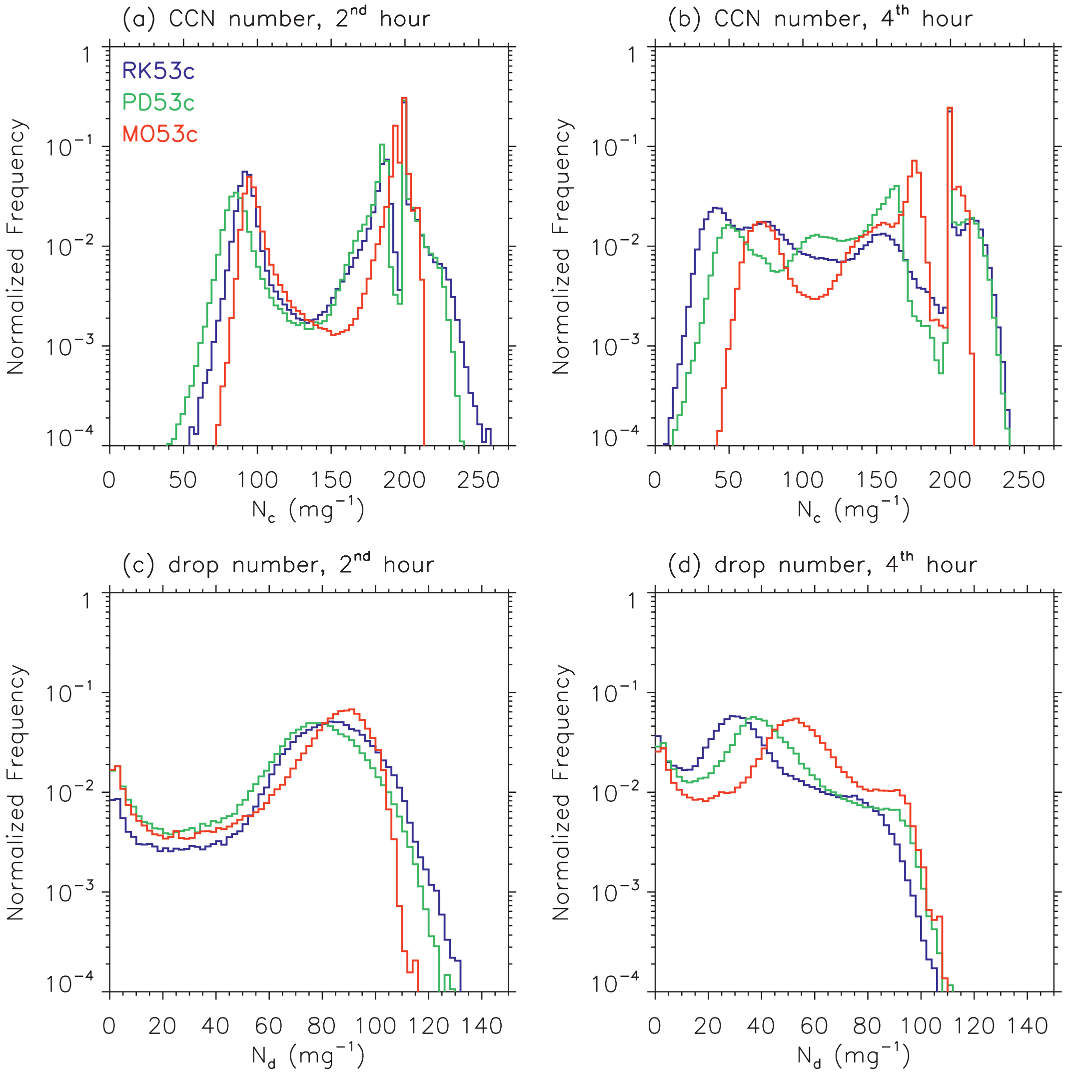

FIG. 2. Histogram of CCN number concentration N_c and cloud droplet plus rain drop number concentration N_d at the end of the second and fourth hour for experiments RK53c, PD53c, and MO53c.

end is from grid cells above clouds. Contribution to the middle part of the histogram is from below-cloud grid cells where CCN have been transported to cloud in updrafts. Overall, the CCN histogram of the RK53c and PD53c cases is broader than that of the MO53c case, at least partly, because of the overshooting and undershooting associated with the RK and PD schemes. A significant number of grids have N_c greater than the initial value of 200 mg^{-1} in both the RK53c and PD53c cases. These grids are located above the cloud top (inversion base) where sharp gradients in CCN exist. The maximum N_c reaches 325 (249) mg^{-1} in the RK53c (PD53c) case. The N_d histogram is also narrower in MO53c at the second hour when feedbacks from cloud physical processes do not dominate the effect of advection errors. By the fourth hour, when physical processes have been fully involved, CCN in the boundary layer are depleted by activation and collection processes differently in the three cases. Shifts in the frequency peaks are clearly seen. The same trends hold for cloud droplets. The median value of N_d at the second (fourth) hour for RK53c, PD53c, and MO53c is 82 (32), 76 (39), and 85 (52) mg^{-1}, respectively. The relative difference in median value caused by the advection scheme changes from about 12% (second hour) to 63% (fourth hour) in 2 h, indicating a substantial impact of the numerical errors on cloud properties.

The basic RK scheme and the PD limiter may lead to a misrepresentation of the cloud physical and dynamical processes. For example, as shown by the horizontally averaged vertical profiles in Fig. 3c, CCN number concentration in the three cases has different degrees of

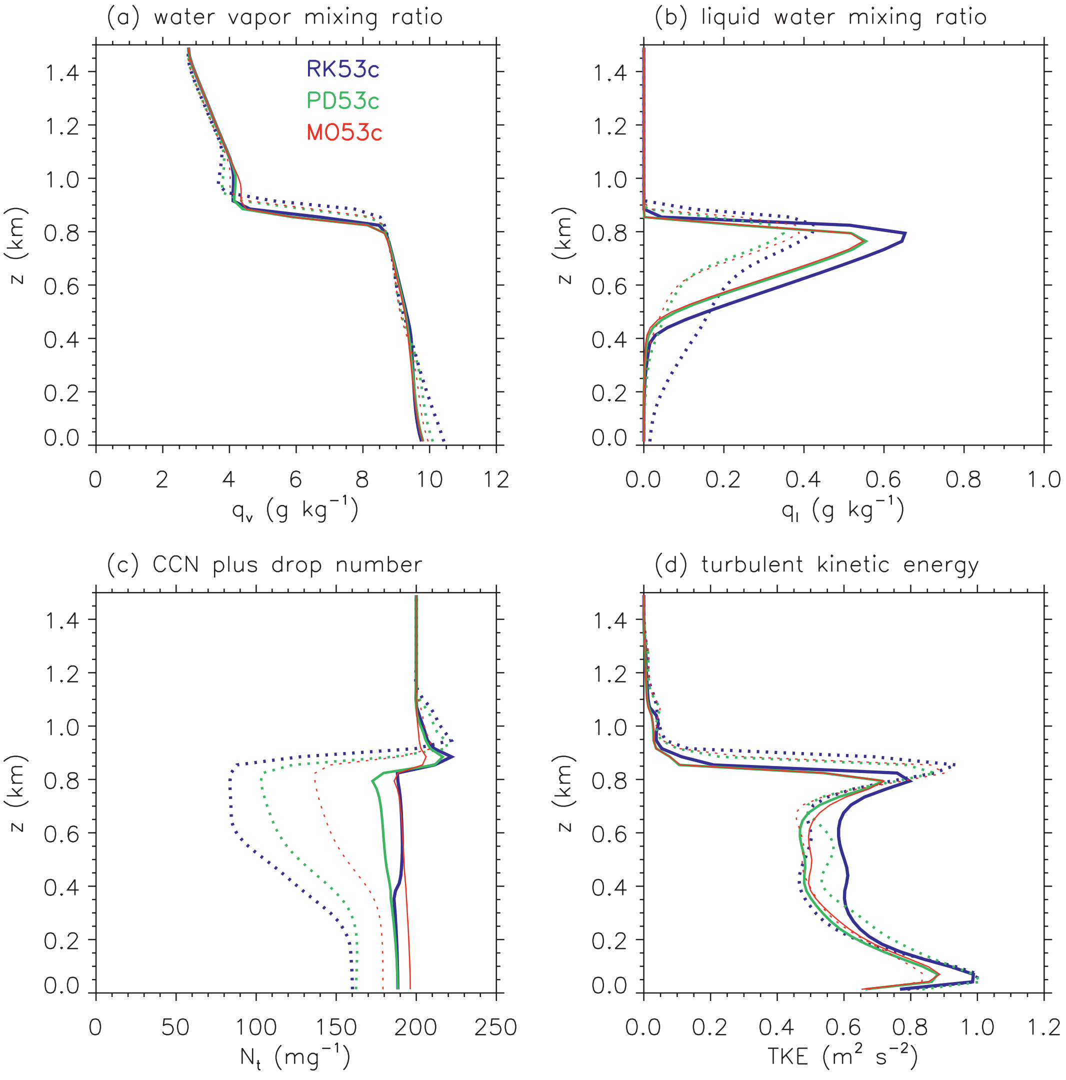

FIG. 3. Vertical profile of domain-average (a) water vapor mixing ratio q_v, (b) liquid water mixing ratio q_l, (c) total particle number concentration N_t ($=N_c + N_d$), and (d) TKE. Profiles are hourly averages over the second (solid lines) and the fourth hour (dotted lines).

enhancement above 0.8 km relative to the initial number concentration of 200 mg^{-1}. The enhancement is associated with the sharp gradients in N_c and N_d at cloud top, only part of which could derive from a physical process, namely evaporation of detrained cloud droplets. With the monotonic limiter the maximum enhancement increases from 3% at the second hour to 5% at the fourth hour because of an accumulation of CCN above cloud. However, with the basic RK scheme and the PD limiter the enhancement is overpredicted because of the combined numerical errors associated with the advection of both N_c and N_d. The maximum enhancement in the horizontally averaged N_c is 8% (11%) and 10% (11%) in PD53c (RK53c) for the second and the fourth hour. Locally, this enhancement in PD53c and RK53c has much larger variations than in MO53c, exceeding 20% above strong updrafts. As a result, relative to MO53c, total particle number concentrations N_t ($=N_c + N_d$) in and below cloud are underpredicted by 5% (184 versus 194 mg^{-1}) in PD53c for the second hour, and the reduction further increases to 16% (141 versus 164 mg^{-1}) for the fourth hour when more feedbacks are involved. In the second hour, N_t in RK53c is higher than in PD53c, both in and above cloud. This must be caused by an additional source of particles induced by removal of negative values. However, in the fourth hour, in-cloud N_t drops drastically to an even lower value. This odd behavior of N_t in RK53c is explained next.

c. *Impact of advection schemes on aerosol–cloud interactions*

Also shown in Fig. 3 are vertical profiles of water vapor mixing ratio q_v, liquid water mixing ratio q_l, and TKE. Without the monotonic limiter, overshooting and undershooting in q_v occurs near the inversion. Although there is no notable decrease in q_v, RK53c has more liquid water in clouds than the other cases. This excess of water substance must be due to the removal of negative q_l that was produced by advection. Subsequently, the collision–coalescence process is accelerated, and larger drizzle drops start to fall below the cloud base and reach the surface during the fourth hour in RK53c, which results in further reductions in CCN and the cloud droplet number. This explains why N_t drops drastically from the second hour to the fourth hour in RK53c as shown in Figs. 2 and 3. Moreover, evaporation of drizzle drops adds more water vapor to the subcloud layer, which, together with evaporative cooling, triggers other changes in cloud physical and dynamical processes. Differences in the TKE profile between the cases shows evidence of the impact of the advection scheme and feedbacks to turbulent dynamics. Below 0.2 km, TKE tends to decrease with time in PD53c and MO53c, while the relative increase in TKE with time in the RK53c case is related to drizzle. When comparing horizontal snapshots of TKE and rainwater fields (not shown), TKE maxima are seen in grid cells that surround grids containing rainwater. The overall stronger TKE in RK53c is due to feedbacks from longwave radiative forcing, which is proportional to cloud liquid water content.

The above results have demonstrated that numerical dispersion errors in the basic RK scheme and the PD limiter have a substantial impact on cloud microphysical properties due to both direct transport and feedbacks through physical, dynamical, and radiative processes. Figure 4 shows how the different advection schemes influence cloud macrophysical properties that are often used to quantify aerosol–cloud interactions. When comparing the temporal mean in different cases, we use the average over the last 4 h. First, the basic RK scheme erroneously adds a significant amount of liquid water to the domain. The mean LWP in RK53c is about 1.5 times larger than that in PD53c and MO53c. This triggers and assures the strong persistent surface drizzle seen in Fig. 4f. As a result of depletion of CCN in the drizzle processes, N_d is significantly reduced, approaching the threshold value of 20 mg^{-1} suggested as the definition of "cloud" by Ackerman et al. (2009). The PD flux limiter tends to underpredict LWP, cloud fraction, N_d, and cloud albedo in both the clean and polluted cases. All these quantities decrease with time faster than in corresponding simulations with the monotonic flux limiter. The most direct explanation is that too many CCN are moved directly from the cloud layer to the free troposphere as a result of the numerical errors seen in Fig. 3. Some feedback mechanisms contribute to this as well. For example, fewer, but larger drops collide and coalesce more efficiently, further reducing CCN; once the stratiform cloud breaks up, more cloud edges and sharp gradients of microphysical quantities, potentially problematic regions, are created. After clouds start to deepen at about 6.5 h in PD53c, LWP increases and a significant amount of drizzle reaches the surface, showing a similar behavior to that in RK53c.

How do the different flux limiters impact aerosol effects on clouds? The basic RK scheme alone is excluded in the comparison because it is obviously problematic in this application. Table 1 summarizes the change of mean N_d and cloud albedo α_c due to different advection schemes and the aerosol perturbation derived from the last 4-h averages in Fig. 4. The left two columns compare the N_d and α_c response to the aerosol perturbation when different flux limiters are used. There are significant and seemingly inconsistent changes in the two quantities. For example, even though the PD limiter gives a 15% [(0.33–0.28)/0.33] *larger* increase in α_c than the monotonic limiter does, it is associated with a 7% *smaller* increase in N_d (125.5 versus 134.7 mg^{-1}) as a result of the complex feedbacks from changes in cloud droplet size and LWP.[2] Overall, the 0.05 (0.33 versus 0.28) change in $\Delta\alpha_c$ caused by the different advection schemes is not substantial, but it is interesting to understand the source of this difference. The right two columns show that the PD scheme results in both smaller N_d and α_c for both clean and polluted conditions. In the clean case, α_c is more significantly underpredicted (22%) by PD as a result of a lower N_d and an overactive drizzle process (see also Fig. 4f). By suppressing drizzle, the addition of CCN generates a significant increase in α_c ($\Delta\alpha_c = 0.33$; left column). For the MO scheme, drizzle is less active and albedo does not drop as low as in PD53c. Thus, the addition of CCN generates a smaller $\Delta\alpha_c = 0.28$. Therefore the disparity in sign change between $\Delta\alpha_c$ and ΔN_d as a result of the aerosol perturbation (left columns) can be traced to the suppression of an overactive drizzle process in PD53c.

---

[2] Note that for clouds of equal LWP, the cloud optical depth τ_c scales as $N_d^{1/3}$ because τ_c and α_c are approximately linearly dependent at small τ_c, $\alpha_c \propto N_d^{1/3}$. Therefore, percentage changes in α_c should be about 1/3 of the percentage changes in N_d, but of the same sign. The fact that this is not the case reflects the complexity of these feedbacks.

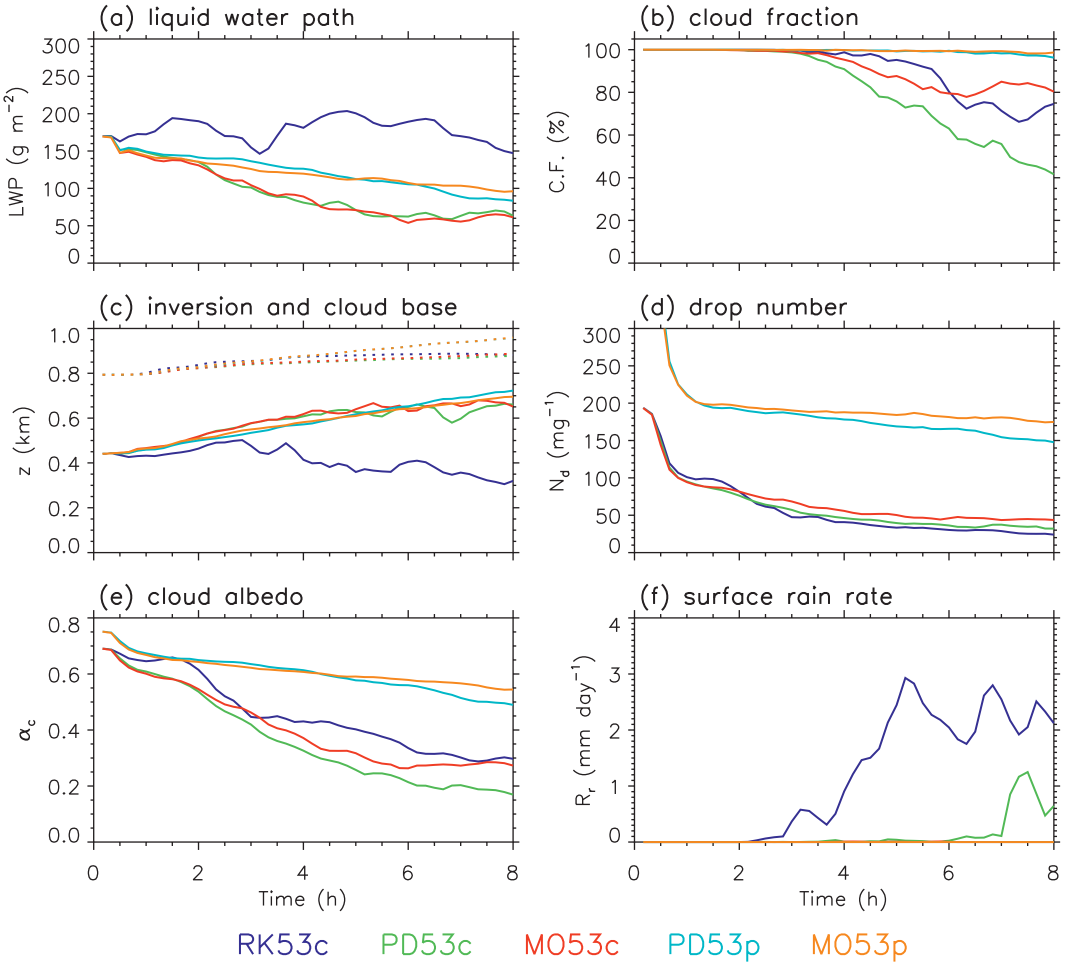

FIG. 4. Time evolution of (a) domain-average LWP, (b) cloud fraction (CF), (c) domain-average inversion base height (dotted line) and cloud-base height (solid line), (d) cloud-average drop number N_d, (e) domain-average cloud albedo α_c, and (f) domain-average surface rain rate R_r for the five experiments as indicated in the legend. Cloudy columns are defined by an optical depth threshold of 2 for the cloud fraction calculation, while a criterion of $N_d \geq 20$ mg^{-1} is applied when calculating cloud-average N_d, following Ackerman et al. (2009).

Finally, if we compare the sensitivity of cloud albedo to the change in droplet number concentration (i.e., $\Delta\alpha_c/\Delta N_d$), the PD scheme overpredicts it by 20% (0.0026 versus 0.0021).

5. Conclusions

A monotonic flux limiter in combination with the basic third-order Runge–Kutta time-integration scheme has been introduced into the ARW for scalar advection. Its performance for scalar transport in fine-resolution ARW simulations has been evaluated against the basic RK scheme and an existing positive-definite flux limiter. Without any flux limiter the RK scheme produces spurious oscillations and negative values in scalar mixing ratios, which is worse near sharp gradients. Simple removal of nonphysical negative mixing ratios in the RK scheme destroys the scalar conservation by adding a spurious scalar source. These numerical errors can contaminate active scalars directly through the advection process and indirectly through feedbacks to physical processes. Simulation results show that adding extra

TABLE 1. Change in mean drop number concentration (N_d, mg^{-1}) and cloud albedo (α_c) over the last 4 h due to an aerosol perturbation and different advection schemes.

	Polluted − clean		Monotonic − PD	
	PD	Monotonic	Clean	Polluted
ΔN_d, mg^{-1}	125.5	134.7	9.5 (20%)	18.7 (10%)
$\Delta\alpha_c$	0.33	0.28	0.06 (22%)	0.03 (5%)
$\Delta\alpha_c/\Delta N_d$, mg	0.0026	0.0021	—	—

cloud water by simply setting negative values to zero causes a significant increase in the surface rain rate, which enhances depletion of CCN and reduction of cloud droplet number concentration, leading to a further enhancement in precipitation. Applying the positive-definite flux limiter not only removes the negative values while conserving water mass but also reduces the spurious oscillations. However, amplification of local maxima is still as large as 20% in our tests, which cannot be ignored in cloud microphysics. The dispersion errors associated with the basic RK scheme and the PD limiter may lead to a misrepresentation of cloud physical and dynamical processes.

The monotonic limiter is formulated to correct the generally accurate, but dispersive solutions given by the high-order RK scheme using the low-order diffusive yet monotonic flux. It effectively minimizes the dispersion errors. In spite of this, little significant enhancement of numerical diffusion error is noticed when using fifth- (third) order horizontal (vertical) accuracy for spatial derivatives in advection schemes. The sharp gradients in scalar mixing ratios are preserved reasonably well. In contrast, the monotonic limiter applied to a high-even-order accurate scheme gives more diffusive solutions because the high-even-order scheme is more dispersive and more weight has to be put on the low-order diffusive flux when doing flux renormalization. Computationally, for the number of scalars in this study (basic model variables plus 7 others in the double-moment microphysical scheme), the monotonic limiter is 8% more costly (7% for the PD limiter) than the basic RK scheme.

The impact of different flux limiters on assessing aerosol–cloud interactions is examined using the simulation results. Overall, the PD flux limiter tends to underpredict liquid water path, cloud fraction, cloud droplet number concentration, and cloud albedo in both clean and polluted cases. The PD limiter results in 20% (10%) fewer cloud droplets than the monotonic limiter when the initial CCN is 200 (500) mg^{-1}, and 22% (5%) smaller α_c. On average, the PD limiter overpredicts cloud susceptibility ($\Delta\alpha_c/\Delta N_d$) by 20%. Underprediction of cloud droplet number concentration in PD53c tends to trigger the formation of precipitation, leading to a potentially large impact on cloud albedo change.

The results in this study suggest that the RK scheme with a monotonic flux limiter using fifth- (third) order horizontal (vertical) accuracy is recommended for scalar advection in the ARW-WRF, at least for the fine-resolution cloud modeling presented here. Future work should be done to assess how the monotonic flux limiter may improve simulation results in other applications such as chemical transport and cloud-scale modeling with bin representation of aerosol and water particles.

Acknowledgments. We acknowledge support from NOAA's Climate Goal. Hailong Wang was supported by the Cooperative Institute for Research in Environmental Sciences (CIRES) Visiting Fellowship. We thank Hongli Jiang, Adrian Hill, Mary Barth, and Chin-Hoh Moeng for thoughtful discussions. The comments of two anonymous reviewers helped to improve the manuscript.

APPENDIX

Evaluation of the ARW for Large-Eddy Simulations

Given its design, the ARW should be suitable for large-eddy simulation. Moeng et al. (2007) demonstrated the performance of an earlier version of the ARW-WRF (version 2.1) with the basic Runge–Kutta scheme for LES of boundary layer turbulence. Results are comparable to observations and those of other LES studies. To examine how well the new version (version 3.0) of the ARW along with the monotonic flux limiter and the double-moment microphysical scheme (Feingold et al. 1998) represent moist convection and boundary layer clouds, the model is configured closely following the DYCOMS-II RF02 LES intercomparison specifications, and simulation results are evaluated against those of the intercomparison (available online at http://gcss-dime.giss.nasa.gov/dycoms-ii/modsim_dycoms-ii_gcss7-rf02.html). The same initial sounding, surface fluxes, longwave radiative flux parameterization, and large-scale subsidence are used. The model domain is 6.4 × 6.4 × 1.5 km^3 with horizontal (vertical) grid spacing of 50 (12) m.

In the intercomparison study (Ackerman et al. 2009), LES models with single-moment microphysical schemes that only predict mass mixing ratio prescribe cloud droplet number concentration $N_d = 55\ \mathrm{cm}^{-3}$. Otherwise, as in our double-moment microphysical scheme, N_d is a prognosed variable and evolves with time based on microphysical and dynamical processes. We run a simulation N120 with initial CCN number concentration of 120 cm^{-3} for 6 h. The average N_d over the last 4 h is 47 cm^{-3}, which is close to the lower bound of the ensemble range.

Vertical profiles of model variables and derived higher-order fluxes are plotted in Figure A1 along with ensemble results of the DYCOMS-II RF02 LES intercomparison. All quantities except for the variance of vertical velocity (w) and subcloud rain rate lie within the ensemble range. Model variables such as total water mixing ratio q_t and liquid water potential temperature θ_l,

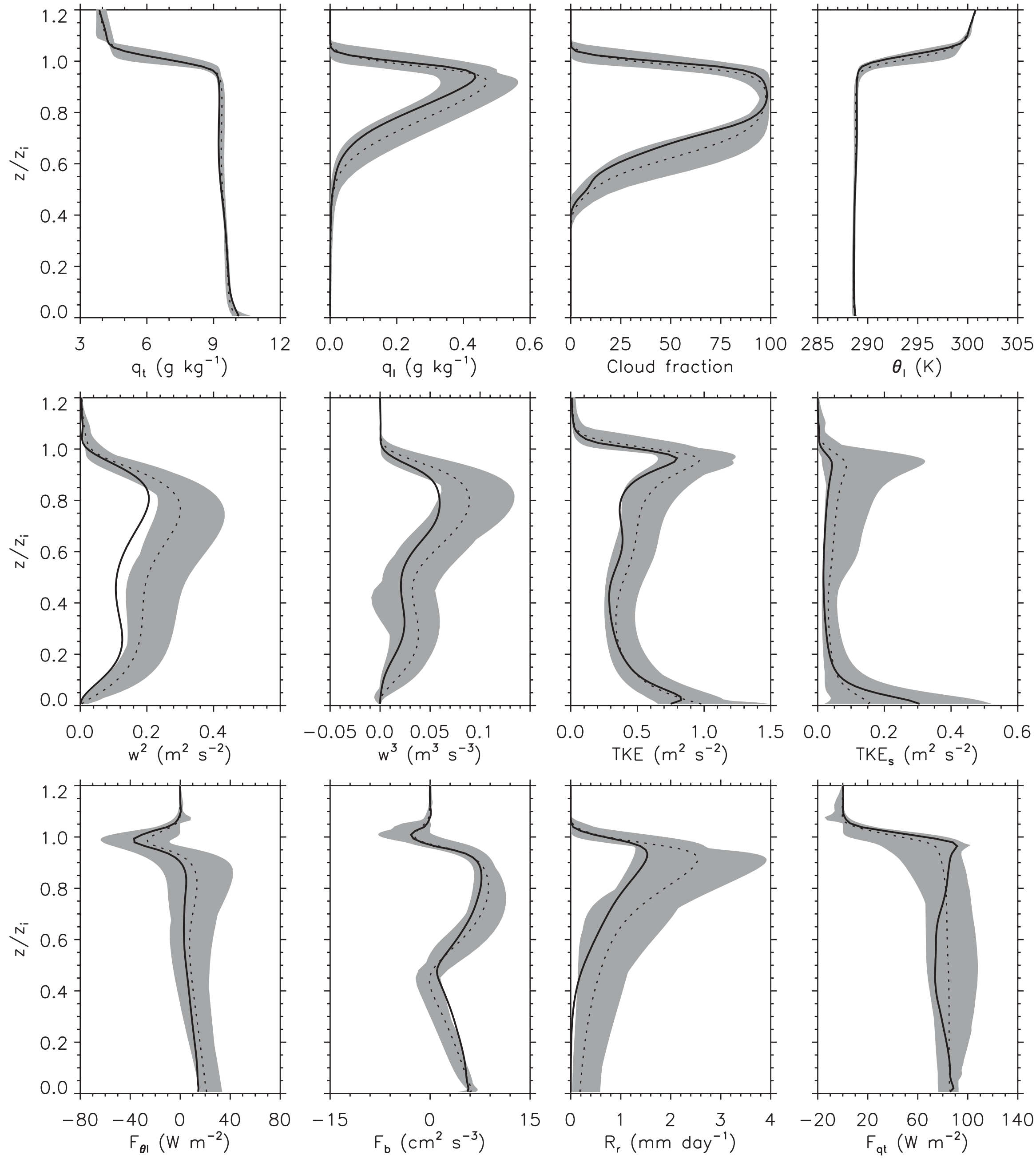

FIG. A1. Vertical profiles of total water mixing ratio q_t, liquid water mixing ratio q_l, cloud fraction, liquid water potential temperature θ_l, variance of vertical velocity w^2, third moment of vertical velocity w^3, TKE, subgrid-scale TKE TKE$_s$, θ_l flux $F_{\theta l}$, buoyancy flux F_b, rain rate R_r, and total water flux F_{qt}. Shaded areas are ensemble ranges and dotted lines are corresponding ensemble means, which are adapted from the DYCOMS-II LES intercomparison (Ackerman et al. 2009). Solid lines are results from simulation N120.

match the corresponding ensemble mean especially well. The *w* variance and rain rate are also two quantities that the ensemble members agree the least on, as indicated by the relatively large spread. The underprediction of *w* variance and rain rate is consistent with the persistent drop of liquid water path (LWP), shown in Figure A2. The domain-average LWP in N120 is about 90 g m^{-2}. It is within the ensemble range but noticeably smaller than the ensemble mean of 112 g m^{-2}. Sensitivity tests show that *w* variance is enhanced when LWP increases with increasing N_d. This is mainly because radiative cooling, which drives vertical motions in cloud, is enhanced by higher LWP.

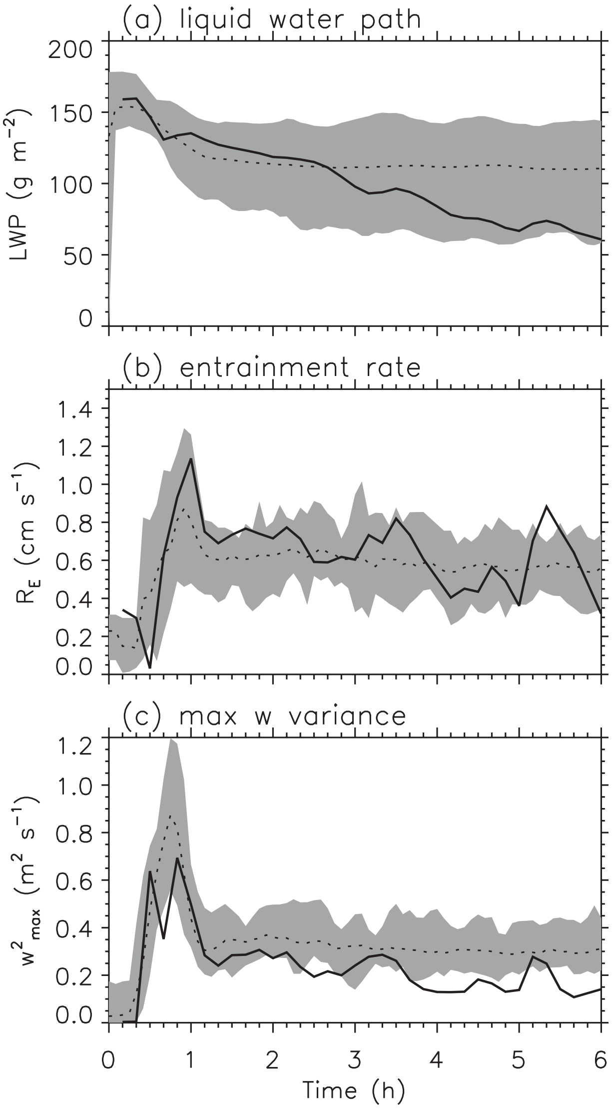

FIG. A2. Time evolution of domain-average LWP, entrainment rate, and maximum variance of vertical velocity. Denotations of lines and shading are the same as in Fig. A1.

Also shown in Fig. A2 is the time evolution of the entrainment rate and maximum *w* variance. Relative to the ensemble mean, the entrainment rate is overpredicted and the maximum *w* variance is underpredicted (as also shown in Fig. A1). The overentrainment of dry air above the boundary layer may have caused the persistent decrease of LWP, and therefore, the underprediction of *w* variance and the rain rate.

Finally we note that the only difference between our simulation setup and the prescribed conditions is that we fixed $\Delta z = 12$ m whereas most participants in the intercomparison study used a stretched grid. Intercomparison study results using stretched vertical grid structure showed a significant increase in LWP and precipitation when vertical grids were more stretched in and below clouds, and this alone may well explain the lower LWP produced by our simulations.

REFERENCES

Ackerman, A. S., and Coauthors, 2009: Large-eddy simulations of a drizzling, stratocumulus-topped marine boundary layer. *Mon. Wea. Rev.,* **137,** 1083–1110.

Anderson, D., and B. Fattahi, 1974: A comparison of numerical solutions of the advective equations. *J. Atmos. Sci.,* **31,** 1500–1506.

Feingold, G., R. Boers, B. Stevens, and W. R. Cotton, 1997: A modeling study of the effect of drizzle on cloud optical depth and susceptibility. *J. Geophys. Res.,* **102,** 13 527–13 534.

——, R. L. Walko, B. Stevens, and W. R. Cotton, 1998: Simulations of marine stratocumulus using a new microphysical parameterization scheme. *Atmos. Res.,* **47–48,** 505–528.

Grell, G. A., S. E. Peckham, R. Schmitz, S. A. McKeen, G. Frost, W. C. Skamarock, and B. Eder, 2005: Fully coupled online chemistry within the WRF model. *Atmos. Environ.,* **39,** 6957–6975.

Moeng, C.-H., J. Dudhia, J. B. Klemp, and P. P. Sullivan, 2007: Examining two-way grid nesting for large eddy simulation of the PBL using the WRF model. *Mon. Wea. Rev.,* **135,** 2295–2311.

Ovtchinnikov, M., and R. C. Easter, 2009: Nonlinear advection algorithms applied to interrelated tracers: Errors and implications for modeling aerosol–cloud interactions. *Mon. Wea. Rev.,* **137,** 632–644.

Skamarock, W. C., 2006: Positive-definite and monotonic limiters for unrestricted-time-step transport schemes. *Mon. Wea. Rev.,* **134,** 2241–2250.

——, and M. L. Weisman, 2009: The impact of positive-definite moisture transport on NWP precipitation forecasts. *Mon. Wea. Rev.,* **137,** 488–494.

——, and Coauthors, 2008: A description of the Advanced Research WRF version 3. NCAR Tech. Note NCAR/TN-475+STR, 113 pp.

Stevens, B., and Coauthors, 2003: Dynamics and chemistry of marine stratocumulus—DYCOMS-II. *Bull. Amer. Meteor. Soc.,* **84,** 579–593.

——, G. Vali, K. Comstock, M. C. vanZanten, P. H. Austin, C. S. Bretherton, and D. Lenschow, 2005: Pockets of open cells (POCs) and drizzle in marine stratocumulus. *Bull. Amer. Meteor. Soc.,* **86,** 51–57.

Zalesak, S. T., 1979: Fully multidimensional flux-corrected transport algorithms for fluids. *J. Comput. Phys.,* **31,** 335–362.